Efficient removal of lead ions from aqueous solutions using ZnSe/ZnO/Bio-$CaCO_3$

Yi Yan, Shuai Yang, Feng Jiang, Yuwei Luo, Hejun Gao and Yunwen Liao

ABSTRACT

The sheet-like adsorbent of the eggshell wastes was prepared by the thermal hydrolysis method. The structure of the adsorbent was characterized by scanning electron microscope, Brunauer-Emmett-Teller, X-ray diffraction, transmission electron microscope, and X-ray photoelectron spectrometer. The adsorption capacity was investigated in a Pb^{2+} solution. The effects of initial pH, salt concentration, contact time, and adsorbate concentration on the adsorption of lead ions were investigated in detail. The morphology of the adsorbent was sheet-like microspheres. Zinc selenide/zinc oxide could be uniformly loaded onto the eggshell waste surface, which could effectively enhance the specific surface area of the eggshell wastes. The adsorption kinetics and isotherm followed the pseudo-second-order and Langmuir–Freundlich isotherm model, respectively. The synthesized adsorbent showed a maximum lead adsorption capacity of 1,428.78 mg/g at room temperature. Ion-exchange was the main adsorption mechanism.

Key words | eggshell wastes, lead ions, removal, ZnSe

Yi Yan†
Shuai Yang†
Feng Jiang
Yuwei Luo
Hejun Gao (corresponding author)
Yunwen Liao
College of Chemistry and Chemical Engineering,
China West Normal University,
Nanchong 637000,
China
E-mail: *hejun_gao@126.com*

Hejun Gao
Institute of Applied Chemistry,
China West Normal University,
Nanchong 637000,
China

†Yi Yan and Shuai Yang contributed equally to this work.

INTRODUCTION

With the development of modern industry, much wastewater containing heavy metals is discharged into the environment. It is a serious threat to human health through the food chain (Yang *et al.* 2019). The lead ion is one of the common and highly toxic heavy metal ions. It could seriously endanger human organs, nervous system, and blood system, and even cause death (Ren *et al.* 2019). Lead ion pollution mainly comes from lead mining, electronics assembly plants, urban rainwater runoff, etc. The World Health Organization stipulates that the concentration of lead ions in drinking water must be less than 0.01 mg/L (Venkateswarlu & Yoon 2015). So far, there are many techniques and methods used to deal with lead contaminants, such as adsorption, membrane separation, etc. (Chen *et al.* 2019; Dong *et al.* 2019). Adsorption technology, which has simple operation, high efficiency, and low-cost advantages, is widely used in lead ions' wastewater treatment. The accumulation and bonding of heavy metal ions at the solid-liquid interface can be studied by adsorption (Karthik & Meenakshi 2015). Especially, non-toxic or low-toxic ions can remove highly toxic ions from aqueous solutions by ion exchange in the adsorption process (Ma *et al.* 2019).

Many inorganic materials are applied to remove heavy metal ions from aqueous solution, such as ZnO and ZnSe. Due to their excellent cation exchange capacity, they are considered one of the most promising adsorbent materials. The adsorption capacity of the lead ions on ZnO could reach 833 mg/g in the early report (Xu *et al.* 2016). It is difficult to separate adsorbent from the aqueous solution because of their nano-size and high surface hydrophilicity. The metal oxide is retained in the water for a long time, which is harmful to human health (Choi *et al.* 2019). The chemical bonds of ZnSe are weaker than ZnO, implying that the ion-exchange capacity of ZnSe is greater than ZnO. Moreover, the nanomaterials were applied to improve adsorption performance in wastewater treatment (Wang *et al.* 2018b; Chen *et al.* 2019; Yin *et al.* 2019). Recently, elastomeric nanocomposite foams containing ZnSe were successfully prepared, and were used to remove lead ions from water (Chavan *et al.* 2015). More than 90% of lead ions could be removed within 1 h. However, it was quite expensive and complicated to synthesize, which limits its industrial application.

doi: 10.2166/wst.2020.081

Eggshells are a waste of agricultural products whose composition is Bio-$CaCO_3$, which has a porous interface, is green, cheap, and easy to get, etc. It has attracted scholar's attention. Calcium ions are easily ion-exchanged with lead ions in aqueous solutions to achieve efficient wastewater treatment (López-Marzo *et al.* 2012). Eggshells are also a large-sized porous support. Eggshells could remove contaminants from aqueous solutions, such as methylene blue, Cr(III), Ca^{2+}, Cd^{2+}, Pb^{2+}, and Li^{+} (Pettinato *et al.* 2015; De Angelis *et al.* 2017; Tizo *et al.* 2018; Wang *et al.* 2018a). However, the adsorption capacity was low. In this work, ZnSe/ZnO was loaded onto the eggshell to obtain a composite material with high adsorption performance for lead ions. Its preparation process was relatively simple and inexpensive. It is a new attempt to apply eggshell wastes to treat heavy metal pollution. Especially, after the ion-exchange, the color of composite materials changed from yellow to black, which could be used to identify lead ions in aqueous solutions.

EXPERIMENTAL SECTION

Materials and reagents

Zinc acetate (99.0%), triethanolamine (99–110%), ethanol (99.7%), hydrochloric acid (36.0–38.0%), and hydrazine monohydrate (≥80.0%) were purchased from Aladdin Chemical Co. Sodium selenite pentahydrate (98%), lead nitrate (99.0%), sodium nitrate (99.0%), zinc nitrate hexahydrate (99%), calcium nitrate tetrahydrate (99.0%) were obtained from J&K Scientific Co. All of the chemical reagents were not further purified. The college canteens provided the eggshell waste. The shell membrane was removed in warm water. Then, eggshell wastes (Bio-$CaCO_3$) were washed with distilled water and dried in the oven at 60 °C for 30 minutes. After calcination at the different temperatures (100, 200 and 300 °C, Figure S1, Supplementary Material) for 5 h, the eggshells were ground in an agate mortar and sieved by 200 mesh, and were named Bio-$CaCO_3$(100), Bio-$CaCO_3$(200), and Bio-$CaCO_3$(300), respectively.

Synthesis of ZnSe/ZnO/Bio-$CaCO_3$

ZnSe/ZnO/Bio-$CaCO_3$ was prepared by the thermal hydrolysis method. Firstly, eggshells (1.0 g) and $(CH_3COO)_2Zn.2H_2O$ (1.0 g) were added into 8% $(HOCH_2CH_2)_3N$ aqueous solution and stirred at 90 °C for 2 h. After washing with ethanol solution and drying, white ZnO/Bio-$CaCO_3$ was obtained. Secondly, ZnO/Bio-$CaCO_3$ (0.5 g) and $Na_2SeO_3{\cdot}5H_2O$ (0.25 g) were added into 45% $N_2H_4.H_2O$ aqueous solution at 90 °C for 4 h. After washing, a yellow product was obtained. Finally, the yellow products (ZnSe/ZnO/Bio-$CaCO_3$(100), ZnSe/ZnO/Bio-$CaCO_3$(200) and ZnSe/ZnO/Bio-$CaCO_3$(300)) were annealed to be kept at 400 °C for 2 h. ZnSe/ZnO was synthesized by the same method without eggshells.

Characterization of ZnSe/ZnO/Bio-$CaCO_3$

The morphology and mapping of the element of ZnSe/ZnO/Bio-$CaCO_3$ were characterized using a scanning electron microscope (SEM) (S4800, Hitachi Ltd, Japan). The specific surface area and pore size of ZnSe/ZnO/Bio-$CaCO_3$ were characterized by Brunauer-Emmett-Teller (BET) (version 3.0, Quantachrome Instruments Ltd, USA). The powder X-ray diffraction (XRD) of samples was a Dmax/Ultima IV (Rigaku Corporation, Japan) at a scanning velocity of 5°/min in the range of 5–80°. The morphology of the materials was analyzed using a transmission electron microscope (TEM, Tecnai G2 F20, FEI). The XPS spectrum of the ZnSe/ZnO/Bio-$CaCO_3$-Pb was recorded through an X-ray photoelectron spectrometer (Thermo Fisher k-alpha).

Adsorption experiments

The effect factor, adsorption kinetics and isotherm were investigated by the batch adsorption experiments. The typical adsorption process was as follows. ZnSe/ZnO/Bio-$CaCO_3$ (0.1 g/L) was dispersed in Pb^{2+} aqueous solutions and the values of the initial pH (3.15, 3.78, 4.11, 4.91, and 6.51) were adjusted by HCl solution. The suspension was stirred at room temperature. After filtration, the concentration of Pb^{2+} in the solution was measured by atomic absorption spectrometer (Analytik Jena). The adsorption capacity of q_t (mg/g) was calculated by Equation (1) and the average relative error (ARE) by Equation (2).

$$q_t = \frac{(C_0 - C_t) \times V}{m} \tag{1}$$

$$ARE = \frac{1}{n}\sum_{i=1}^{n}\left|\frac{q_{\exp} - q_{cal}}{q_{\exp}}\right| \tag{2}$$

where C_0 is the initial concentration of Pb^{2+} (mg/L), C_t is the concentration of Pb^{2+} in the adsorption time of t (mg/L), m is the mass of the ZnSe/ZnO/Bio-$CaCO_3$ (g), and V is the volume of the Pb^{2+} solution (L).

RESULTS AND DISCUSSION

Characterization of ZnSe/ZnO/Bio-$CaCO_3$(300)

The microstructures of Bio-$CaCO_3$(300) and ZnSe/ZnO/Bio-$CaCO_3$(300) were analyzed by SEM (Figure 1(a)–1(d)). The surface morphology of the Bio-$CaCO_3$ after calcination at 300 °C is shown in Figure 1(a) and 1(b). It has a multi-layered block structure. After the ZnSe/ZnO loaded onto the Bio-$CaCO_3$(300), the surface morphology of the product had been changed dramatically. It was a petal-like microspheres structure, which was made up of some nanosheets with sizes of about 500 nm. It was obvious that ZnSe/ZnO was successfully loaded onto the surface of the Bio-$CaCO_3$(300), and the change of morphology was beneficial to increase the specific surface area and the active site of the adsorbent. The specific surface area of Bio-$CaCO_3$(300) was about 2 m^2/g. It was increased to ~28 m^2/g after loading ZnSe/ZnO (Table 1 and Figure S2, Supplementary Material). It was not a simple addition of the value of multiple substances, but the structure had changed. The mappings of elements of ion-exchange, such as Ca and Zn, are shown in Figure 1(e) and 1(f) and Figure S3. All the elements ZnSe/ZnO/Bio-$CaCO_3$(300) were uniformly dispersed on the surface, which was beneficial for the adsorption of active sites exposed to contaminated media. Moreover, the content of Ca, Zn and Se was about 39.31%, 14.58%, and 12.43% on the surface of ZnSe/ZnO/Bio-$CaCO_3$(300) (Mapping), respectively. It indicated that the ratio of ZnSe:ZnO: Bio-$CaCO_3$(300) of the adsorbent was about 16:6:39 and most of the ZnO was converted to ZnSe. Especially, the content of Ca on the surface of ZnSe/ZnO/Bio-$CaCO_3$(300) was much larger than that of Zn, which was advantageous for exposure to lead solutions. It implied that the ion-exchange capacity of Ca in the adsorbent could be greater than that of Zn in a specific condition.

The HRTEM of ZnSe/ZnO/Bio-$CaCO_3$(300) is depicted in Figure 1(g) and 1(h). ZnSe/ZnO/Bio-$CaCO_3$(300) was made up of some sheets and their diameters were above 500 nm (Figure 1(g)). This result was very consistent with the morphological analysis of the SEM image. Figure 1(h) shows that ZnSe/ZnO could be well dispersed on the Bio-$CaCO_3$. Three individual nanoparticles show their respective clear lattice fringes. The d-spacing of 0.25, 0.28 and 0.33 nm were attributed to the (110) plane of $CaCO_3$, (100) plane of ZnO and (111) plane of ZnSe, respectively (Chen *et al.* 2016).

The XRD analyses of Bio-$CaCO_3$(100), Bio-$CaCO_3$(200), Bio-$CaCO_3$(300), ZnO/Bio-$CaCO_3$(300), and ZnSe/ZnO/Bio-$CaCO_3$(300) are shown in Figure S4 and Figure 2. It is well known that the main component of Bio-$CaCO_3$ is $CaCO_3$. The characteristic diffraction peak of Bio-$CaCO_3$ at about 23.0°, 29.3°, 31.4°, 35.9°, 39.4°, 43.2°, 47.6°, 48.6°, 56.7°, and 57.5° corresponded to the crystal face of (012), (104), (006), (110), (113), (202), (018), (116), (211) and (122) of Bio-$CaCO_3$, respectively (PDF #05-0586) (Zhang *et al.* 2017). With increasing calcination temperature, the characteristic diffraction peaks at 39.4° and 43.2° gradually enhanced, indicating that the structure of Bio-$CaCO_3$(300) was close to that of pure $CaCO_3$. ZnO was loaded onto the Bio-$CaCO_3$(300). Many new characteristic diffraction peaks were shown in the ZnO/Bio-$CaCO_3$(300), which were due to the crystal face of ZnO (JCPDS No. 80-0074). In the curve of ZnSe/ZnO/Bio-$CaCO_3$(300), the characteristic diffraction peaks at 27.14°, 45.05°, 53.39°, 65.61°, and 72.37° were assigned to the (111), (220), (311), (400) and (331) planes of cubic sphalerite ZnSe, respectively (PDF #00-037-1463 of the ICDD database). This indicated that ZnSe/ZnO/Bio-$CaCO_3$(300) was prepared by the thermal hydrolysis method. It was easy to observe that the characteristic diffraction peaks of ZnO still existed in the ZnSe/ZnO/Bio-$CaCO_3$(300) curve. This implied that ZnO had not been completely converted to ZnSe. While many characteristic diffraction peaks of ZnO were weakened, or even disappeared, indicating that ZnSe was the main form of Zn in the composite. This result agreed with the analysis of mapping.

Effect of pH

To a certain extent, the initial pH of the solution affects the presence of the adsorbate in the aqueous solution. Under alkaline conditions, Pb^{2+} ions are present in the form of $PbOH^+$, $Pb(OH)_2^0$ (Liu *et al.* 2019). In the range of pH < 7.0, lead is present in an aqueous solution in the form of Pb^{2+} ions. It is essential to investigate the adsorption behavior of Pb^{2+} ions in this range. Figure 3(a) and 3(b) show the effect of the initial pH on the adsorption capacity.

Figure 3(a) shows the relationship between the initial pH and the adsorption capacity. It was easy to observe that the adsorption capacity increased with increasing initial pH, especially in the range of pH 3.0 ~ 5.0. In a strong acid solution, most of the adsorption sites on the surface were occupied by the H^+ions in the solution. The positive charge of lead ions produced a huge electrostatic

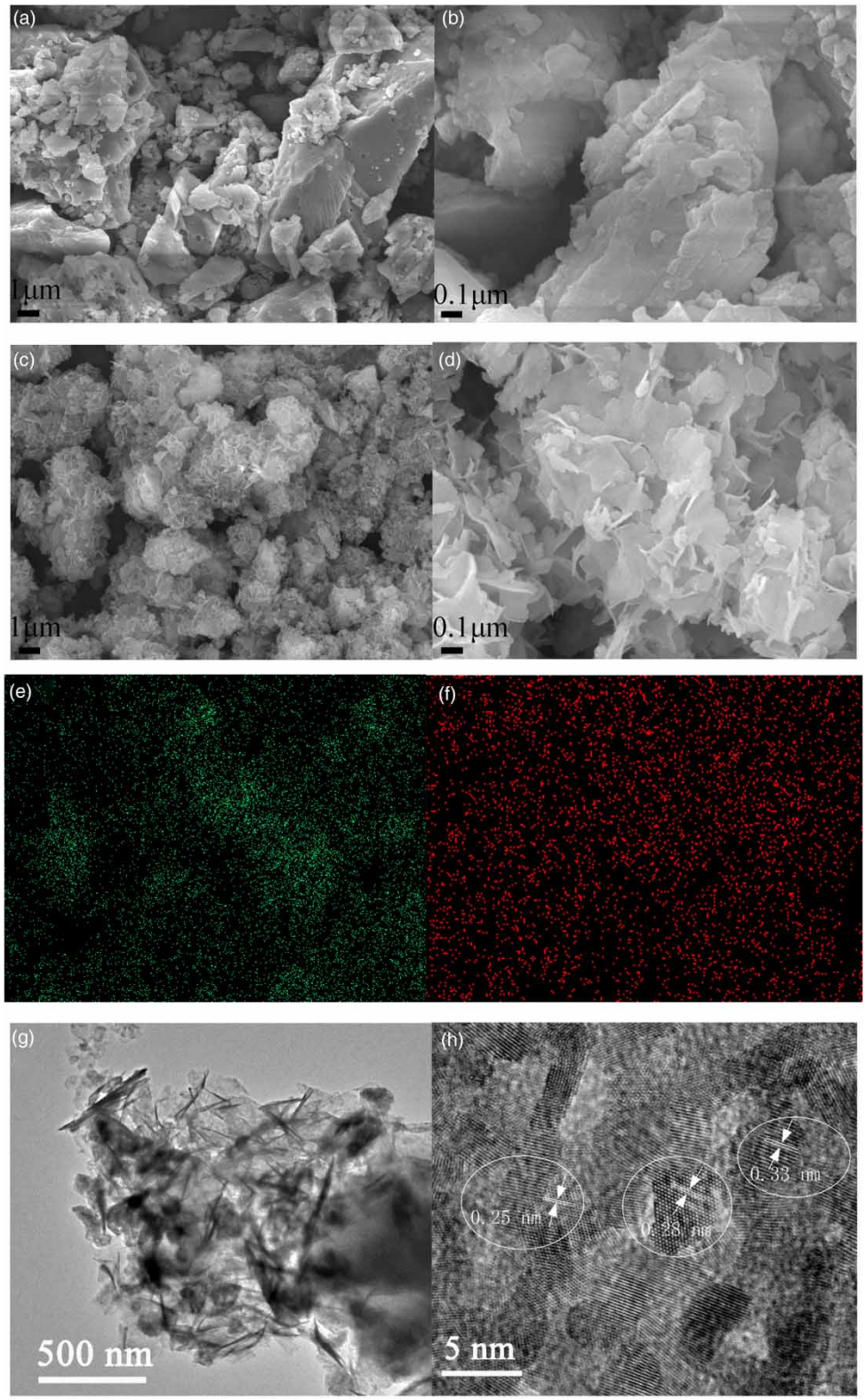

Figure 1 | SEM images of Bio-$CaCO_3$(300) (a and b) and ZnSe/ZnO/Bio-$CaCO_3$(300) (c and d), Mapping of ZnSe/ZnO/Bio-$CaCO_3$(300). (Ca (e), and Zn (f)) and TEM and high-resolution TEM (HRTEM) images of ZnSe/ZnO/Bio-$CaCO_3$(300) (g and h).

Table 1 | The BET result of Bio-$CaCO_3$(300), ZnSe/ZnO and ZnSe/ZnO/Bio-$CaCO_3$(300)

Samples	Surface area (m^2/g)	Pore volume (cm^3/g)	Pore diameter (nm)
Bio-$CaCO_3$(300)	2.055	0.0130	3.825
ZnSe/ZnO	22.46	0.1922	3.407
ZnSe/ZnO/ Bio-$CaCO_3$(300)	28.328	0.3015	30.448

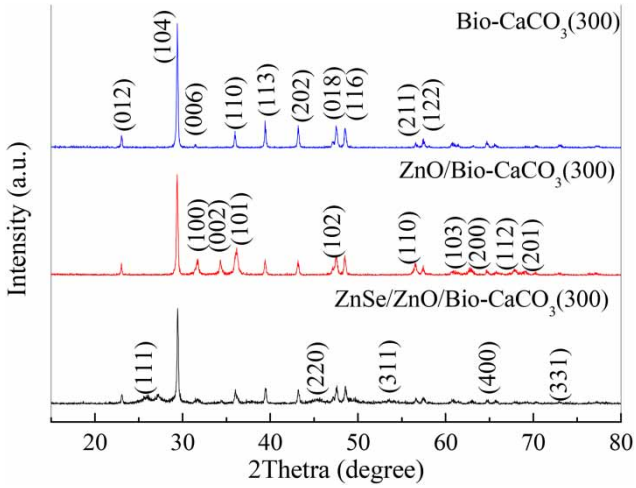

Figure 2 | XRD pattern of Bio-$CaCO_3$(300), ZnO/Bio-$CaCO_3$(300) and ZnSe/ZnO/Bio-$CaCO_3$(300).

repulsion, which seriously hindered the adsorption of lead ions on the material (Gao *et al.* 2019). Above pH 5.0, the adsorption capacity increased slightly. The reason was due to the result of decreased hydrogen ion concentration. This resulted in the ability of the H^+ ions to occupy the adsorption site being reduced and the degree of damage to the structure being weakened. The negative charge on the surface of the adsorbent increased and the electrostatic attraction between Pb^{2+} and ZnSe/ZnO/Bio-$CaCO_3$ was enhanced.

The concentration of H^+ ions in the solution was reduced after adsorption (Figure 3(b)). This implied that the main constituents of the adsorbent were consumed by H^+ ions. It destroyed the surface structure of ZnSe/ZnO/Bio-$CaCO_3$ and reduced the dosage of the adsorbent. Also, the adsorption performance of ZnSe/ZnO/Bio-$CaCO_3$(300) to Pb^{2+} was much better than that of ZnSe/ZnO/Bio-$CaCO_3$(100) and ZnSe/ZnO/Bio-$CaCO_3$(200) at the same pH value, indicating that high-temperature calcination could improve the adsorption performance of ZnSe/ZnO/Bio-$CaCO_3$. The reason was that Bio-$CaCO_3$ could be activated at high temperatures (Seyahmazegi *et al.* 2016). ZnSe/ZnO/Bio-$CaCO_3$(300) was selected as an adsorbent for the following experiments.

Effect of salt

There are many kinds of ions in wastewater. The presence of coexisting ions in water can affect the adsorption capacity of ZnSe/ZnO/Bio-$CaCO_3$. Investigating the effect of salt on the adsorption performance is important. Figure 4 shows the effect of $NaNO_3$, $ZnNO_3$, and $Ca(NO_3)_2$ on the adsorption process of Pb^{2+} by ZnSe/ZnO/Bio-$CaCO_3$.

It was obvious that $NaNO_3$ and $Ca(NO_3)_2$ had a little effect on the adsorption of Pb^{2+} ions in 20 mg/L Pb^{2+} solution, especially $NaNO_3$. Pb^{2+} was more like a typical soft acid ion (boundary soft) and Se^{2-} (soft alkaline) interacted more strongly with soft acid ions Pb^{2+} than the hard ion Na^+ (Manos & Kanatzidis 2016). The ion-exchange of ZnSe/ZnO/Bio-$CaCO_3$ in the adsorption process of Pb^{2+}

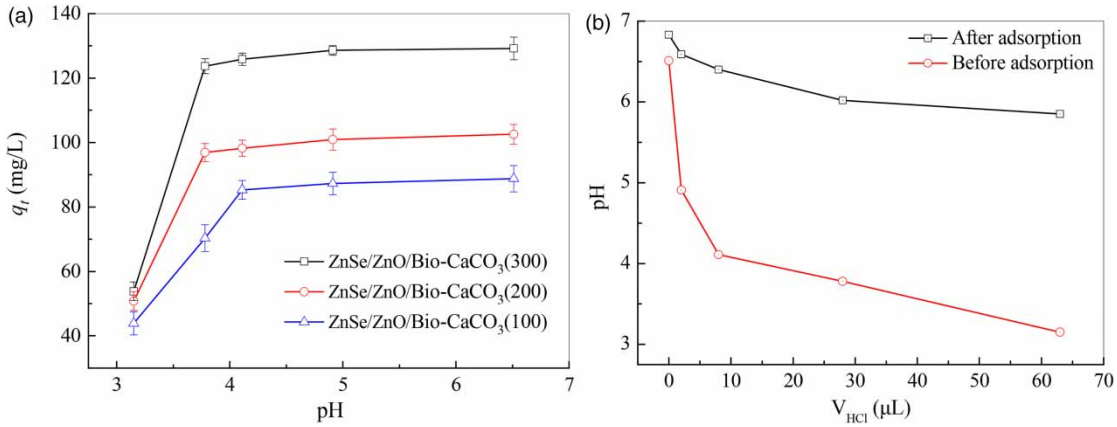

Figure 3 | (a) Effect of pH on the adsorption capacity of Pb^{2+} by ZnSe/ZnO/Bio-$CaCO_3$, (b) the solution pH value before and after adsorption using ZnSe/ZnO/Bio-$CaCO_3$(300) (Dosage = 0.1 g/L, C_0 = 20 mg/L, and t = 6 h).

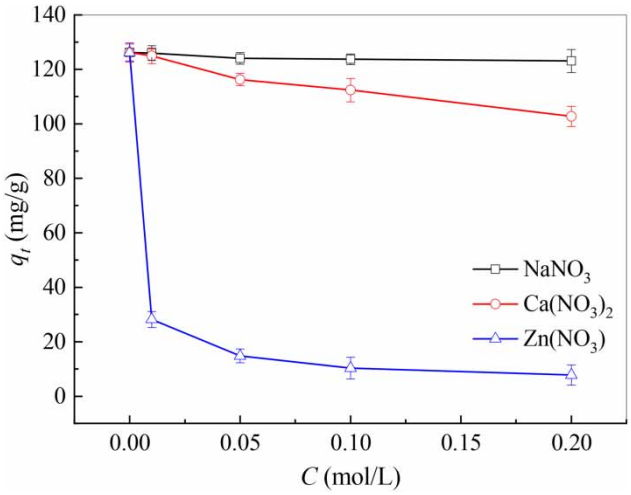

Figure 4 | Effect of salt ($NaNO_3$, $Ca(NO_3)_2$, $Zn(NO_3)_2$) on the adsorption capacity of Pb^{2+} by ZnSe/ZnO/Bio-$CaCO_3$(300) (Dosage = 0.1 g/L, C_0 = 20 mg/L, and t = 6 h).

ions could be summarized as the following two equations (Chavan *et al.* 2015):

$$\text{Bio-CaCO}_3 + \text{Pb}^{2+} \rightarrow \text{PbCO}_3 + \text{Ca}^{2+} \quad (3)$$

$$\text{ZnSe} + \text{Pb}^{2+} \rightleftharpoons \text{Zn}^{2+} + \text{PbSe} \quad (4)$$

In the equation, the increased concentration of Ca^{2+} ions would hinder the ion-exchange of Pb^{2+} ions with Bio-$CaCO_3$. Therefore, the effect of Ca^{2+} ions on the adsorption process was greater than that of Na^{+} ions. While the hindering effect of Ca^{2+} ions was weaker than Zn^{2+} ions, which may be due to the low value of the relative solubility constant K_{sp} of ZnSe. This implied that Zn^{2+} and Pb^{2+} ions were the main ion-exchange reaction during the adsorption process. The result also showed that the Ca^{2+} ions' reactivity was weaker in 20 mg/L Pb^{2+} solution.

Adsorption kinetics

The adsorption kinetic model is used to investigate the influencing factors in the adsorption process and to describe the adsorption mechanism. Figure 5 shows the effect of contact time on the adsorption at 20 mg/L and 200 mg/L of Pb^{2+}, respectively.

The adsorption capacity of Pb^{2+} on ZnSe/ZnO/Bio-$CaCO_3$ increased rapidly in the first 20 min and then the increase gradually reduced until equilibrium in the 20 mg/L Pb^{2+} solution (Figure 5(a)). The equilibrium time was about 1 h. The initial stage of the adsorption rate was quick. This was due to the adsorption process on the surface, which had a large number of adsorption sites (Gao *et al.* 2019). With active adsorption sites gradually occupied, the adsorption rate increased slowly until equilibrium. The C_0 of Pb^{2+} was expanded to 10 times. Then, the equilibrium time was extended to 7 h (Figure 5(b)). This indicated that the adsorption equilibrium time was prolonged with increased initial concentration.

The pseudo-first-order and pseudo-second-order kinetic models were used to analyze the adsorption mechanism (Figure S6a and S6b).

Pseudo-first-order:

$$q = q_e(1 - \exp(-k_1 t)) \quad (5)$$

Pseudo-second-order:

$$q_t = \frac{k_2 q_e^2 t}{1 + k_2 q_e t} \quad (6)$$

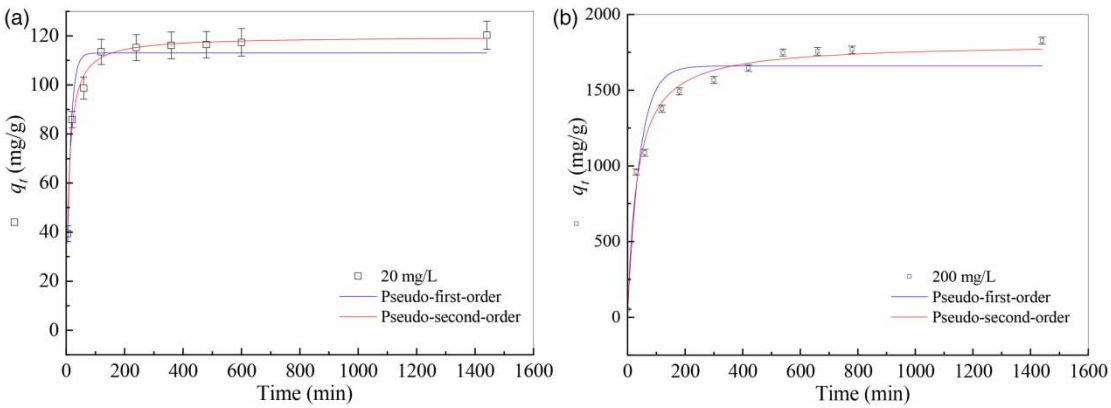

Figure 5 | Effect of contact time on the adsorption of Pb^{2+} at different initial concentration ((a) $C_{Pb^{2+}}$ = 20 mg/L, (b) $C_{Pb^{2+}}$ = 200 mg/L; dosage = 0.1 g/L, pH = 6.51).

Table 2 | Pseudo-first-order kinetics and the pseudo-second-order kinetics model constants of ZnSe/ZnO/Bio-$CaCO_3$(300)

Models	C (mg/L)	k_1	q_e (mg/g)	R^2	q_{exp} (mg/g)	ARE (%)
Pseudo-first-order	20	0.075 ± 0.008	113.06 ± 2.78	0.9613	120.30 ± 5.71	4.8
	200	0.024 ± 0.004	1,659.67 ± 54.77	0.9897	1,827.25 ± 28.05	10.0
		$k_2 \times 10^4$	q_e (mg/g)	R^2		
Pseudo-second-order	20	9.00 ± 0.75	119.76 ± 1.69	0.9894		2.4
	200	0.17 ± 0.015	1,810.47 ± 29.43	0.9982		3.7

where q_e and q_t are the adsorption capacity (mg/g) at equilibrium and at any time t and K_1 (min^{-1}) and K_2 (g/(mg·min)) are the pseudo-first-order and pseudo-second-order rate constants. The kinetic parameters and coefficient of determination (R^2) are shown in Table 2. It was obvious that the R^2 values of the pseudo-second-order model were all above 0.999, which was better than that of the pseudo-first-order model ($R^2 = 0.691$ and 0.922), and the calculated q_t of the pseudo-second-order model was consistent with the experimental data. The pseudo-second-order model could better describe the kinetic data than the pseudo-first-order model, implying that chemisorption was the rate-determining step of adsorption (Li *et al.* 2016) and the adsorption rate was affected by the number of solutes at equilibrium. The adsorption process was primarily controlled by the affinity between Pb^{2+} ions and the binding sites of the ZnSe/ZnO/Bio-$CaCO_3$, which could be ion-exchange (Zhang *et al.* 2015).

Adsorption isotherms

So as to measure the adsorption capacity of ZnSe/ZnO/Bio-$CaCO_3$ and demonstrate the enhancement effect of ZnSe/ZnO on the adsorption of Pb^{2+} ions by Bio-$CaCO_3$, the

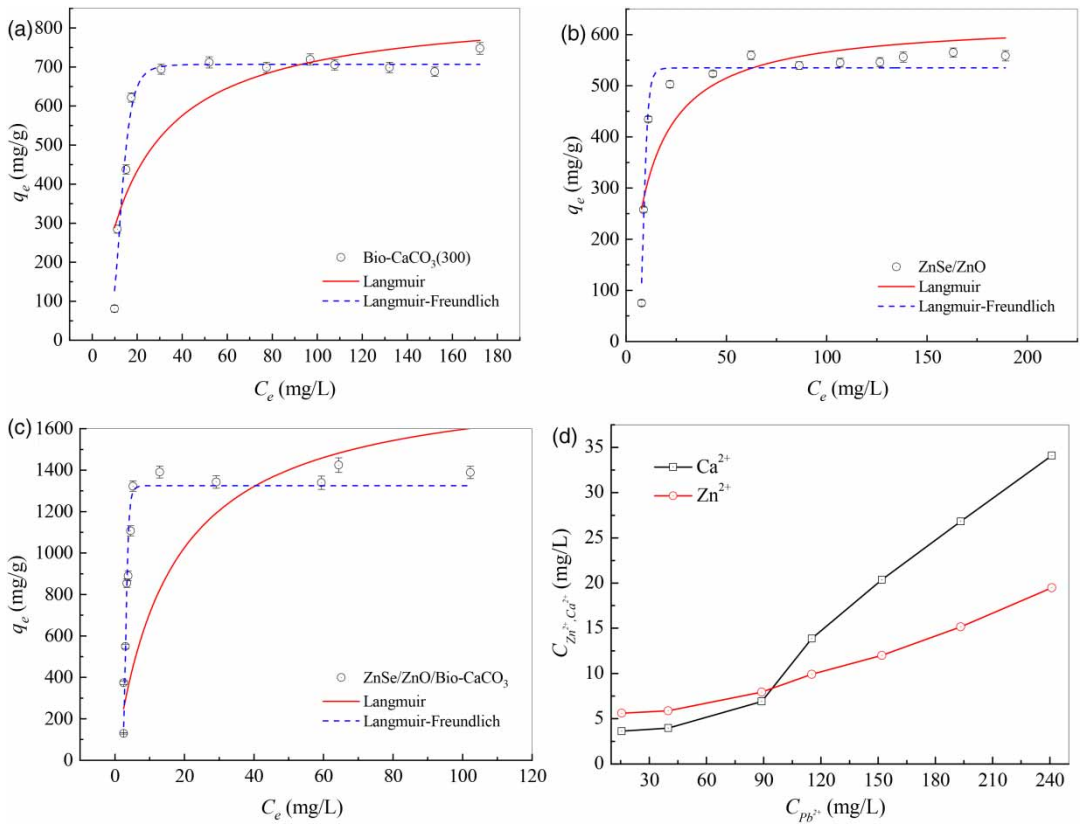

Figure 6 | Adsorption isotherm of Pb^{2+} on Bio-$CaCO_3$ (a), ZnSe/ZnO (b), ZnSe/ZnO/Bio-$CaCO_3$ (c). Concentration of Ca^{2+}, Zn^{2+} and Pb^{2+} ions in the aqueous solution of adsorption isotherm (d) (Dosage = 0.1 g/L, pH = 6.51 and t = 12 h).

Table 3 | Langmuir and Langmuir–Freundlich isotherm constants of Pb^{2+} adsorption on ZnSe/ZnO/Bio-$CaCO_3$(300), ZnSe/ZnO and Bio-$CaCO_3$(300)

Models	Samples	q_m (mg/g)	b (L/mg)	R^2		ARE (%)	q_{exp}
Langmuir	ZnSe/ZnO/Bio-$CaCO_3$(300)	1,854.70 ± 669.09	0.06 ± 0.04	0.5191		84.3	1,424.78 ± 35.10
	ZnSe/ZnO	627.85 ± 59.66	0.09 ± 0.03	0.7040		27.6	549.02 ± 10.11
	Bio-$CaCO_3$(300)	854.89 ± 102.02	0.05 ± 0.020	0.7220		31.1	708.01 ± 15.12
		q_m (mg/g)	b (L/mg)	n	R^2		
Langmuir–Freundlich	ZnSe/ZnO/Bio-$CaCO_3$(300)	1,324.92 ± 110.49	0.31 ± 0.01	0.13 ± 0.02	0.9286	27.1	
	ZnSe/ZnO	534.93 ± 11.24	0.11 ± 0.002	0.12 ± 0.02	0.9699	42.4	
	Bio-$CaCO_3$(300)	706.98 ± 17.67	0.08 ± 0.002	0.18 ± 0.03	0.9702	11.5	

equilibrium data were investigated using the Langmuir and Langmuir–Freundlich adsorption isotherms.

The Langmuir isotherm is suitable for adsorption on a uniform surface. The model is based on the following assumptions. (1) The activity of each adsorption site is the same, and each active site captures only one contaminant. (2) The adsorption energy is constant, and is independent of the surface coverage. (3) After the adsorbate is captured, it will be fixed at the adsorption site (Sarma *et al.* 2016).

The Langmuir–Freundlich isotherm is an extension of the Langmuir model, which is the Freundlich isotherm at low surface coverage or Langmuir isotherms at high surface coverage. Adsorption of heavy metal ions generally follows the Langmuir model, but ion-exchange materials follow the Langmuir–Freundlich isotherm model.

$$q = q_m \frac{bC_e}{1 + bC_e} \tag{7}$$

$$q = q_m \frac{(bC_e)^{1/n}}{1 + (bC_e)^{1/n}} \tag{8}$$

where q (mg/g) is the adsorption capacity of Pb^{2+} at the equilibrium concentration, q_m is the maximum sorption capacity, b (L/mg) is the Langmuir constant, C_e (mg/L) is the equilibrium concentration and n are a constant.

Figure 6(a)–6(c) show the adsorption isotherm of Bio-$CaCO_3$, ZnSe/ZnO and ZnSe/ZnO/Bio-$CaCO_3$ and the equilibrium constants and parameters are shown in Table 3. It was easy to observe that all R^2 values of Langmuir–Freundlich isotherm were superior to the Langmuir isotherm and the maximum adsorption capacity (q_{max}) was close to the experimental value. The Langmuir–Freundlich isotherm could better describe the adsorption isotherm of Pb^{2+} ions. The q_m values of Pb^{2+} could reach 709.78, 542.96 and 1,378.28 mg/g by Bio-$CaCO_3$, ZnSe/ZnO and ZnSe/ZnO/Bio-$CaCO_3$, respectively. The adsorption capacity of ZnSe/ZnO/Bio-$CaCO_3$ was much larger than that of the previously reported adsorbent (Table 4). The reason was as follows. The adsorption capacity was not a simple mathematical sum of q_t of both Bio-$CaCO_3$ and ZnSe/ZnO. It should be attributed to the huge changes in the surface structure of the Bio-$CaCO_3$, which greatly improved the adsorption performance of Bio-$CaCO_3$. Besides, the concentration of Ca^{2+} and Zn^{2+} ions in the adsorption isotherm varied with the initial concentration, as shown in Figure 6(d). At low concentrations, ZnSe/ZnO on the surface of the Bio–$CaCO_3$ was preferentially associated with Pb^{2+} ion exchange. With the increase of Pb^{2+} concentration, Pb^{2+} ions diffused into the ZnSe/ZnO/Bio-$CaCO_3$, and the ion exchange of Ca^{2+} and Pb^{2+} ions gradually played a leading role.

Adsorption mechanism

XRD and XPS investigated the adsorption mechanism of Pb^{2+} on the ZnSe/ZnO/Bio-$CaCO_3$.

Table 4 | Adsorption capacity of different adsorbents for Pb^{2+} ions in aqueous solutions

Adsorbents	q_{max} (mg/g)	References
Chlorella sp. QB – 102	635.8	Li *et al.* (2019b)
CMMB	263.6	Li *et al.* (2019a)
BC/FM	154.94	Zhang *et al.* (2019)
Fe_3O_4/poly($C_3N_3S_3$)	232.6	Fu & Huang (2018)
MIL – 96(Al)	301.5	Mehdinia *et al.* (2018)
NZVI/AC	59.35	Liu *et al.* (2019)
Magnetic biochar/ZnS	367.65	Yan *et al.* (2015)
ZnSe/ZnO/Bio-$CaCO_3$(300)	1,424.78	This work

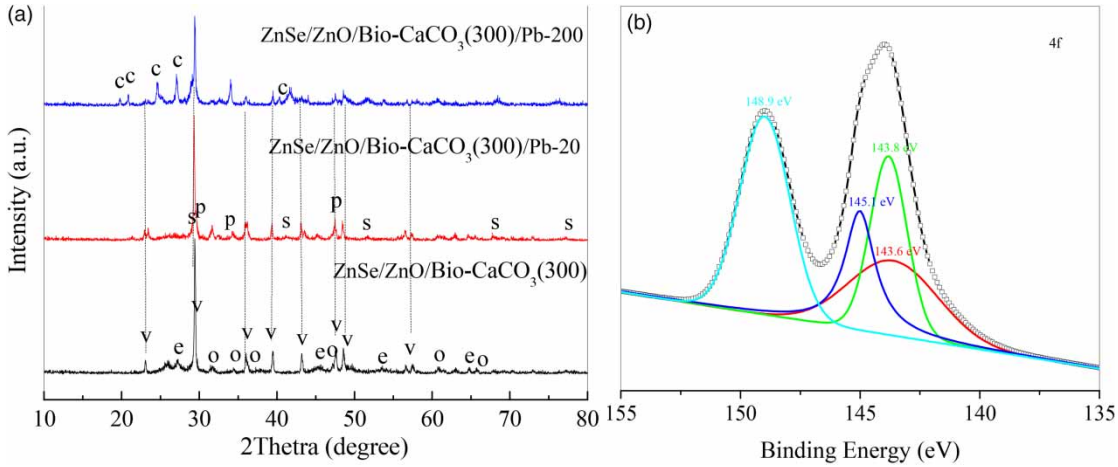

Figure 7 | XRD patterns of ZnSe/ZnO/Bio-$CaCO_3$ and ZnSe/ZnO/Bio-$CaCO_3$/Pb (v Bio-$CaCO_3$, c $PbCO_3$, e ZnSe, s PbSe, o ZnO, p PbO) and high-resolution spectrum of Pb (b).

Compared with ZnSe/ZnO/Bio-CaCOCaCO$_3$, some new peaks were shown in the diffraction peak of ZnSe/ZnO/Bio-$CaCO_3$/Pb-20 (after adsorption in 20 mg/L Pb^{2+} ions), which were due to PbSe (Chavan *et al.* 2015), PbO (Yuan *et al.* 2016) (Figure 7(a)). This indicated that the surface-loaded ZnSe and ZnO were involved in the ion exchange (Equations (3), (4) and (9)).

$$ZnO + Pb^{2+} \rightleftharpoons Zn^{2+} + PbO \quad (9)$$

It was almost impossible to find the diffraction peaks of $PbCO_3$, indicating that Bio-$CaCO_3$ did not participate in the ion exchange. At low concentrations, Pb^{2+} ions did not diffuse into the interior of the adsorbent, which reacted only with the surface layer of ZnSe/ZnO. After increasing the C_0, some significant new diffraction peaks appeared in ZnSe/ZnO/Bio-$CaCO_3$/Pb(200) (after adsorption in 200 mg/L Pb^{2+} ions), which were attributed to the $PbCO_3$ (Yuan *et al.* 2016). At high concentrations, Pb^{2+} ions not only interacted with the surface of the ZnSe/ZnO, but also diffused into the adsorbent, reacting with Bio-$CaCO_3$. The ion exchange between Ca^{2+} and Pb^{2+} ions played an important role in the high concentration solution. The *K*sp of $CaCO_3$ and $PbCO_3$ was about 2.8×10^{-9} and 7.4×10^{-14}, respectively (Zhang *et al.* 2016). Bio-$CaCO_3$ was easily converted to $PbCO_3$ in the high concentration of Pb^{2+} ions solution.

The survey spectrum of ZnSe/ZnO/Bio-$CaCO_3$/Pb(200) exhibited elemental composition (Figure S7). The peaks at 291.28, 352.88, 537.93, 144.07, 61.00, 1,029.27 eV were attributed to C 1s ($CaCO_3$), Ca 2p ($CaCO_3$), O 1s ($CaCO_3$, ZnO), Pb 4f ($PbCO_3$, $Pb(OH)_2$, PbSe), Se 3d (ZnSe, PbSe), and Zn 2p (ZnO, ZnSe), respectively. A high-resolution spectrum of Pb is shown in Figure 7(b). The two peaks at 148.90 and 144.07 eV were due to the 4f of Pb (Zhu *et al.* 2019). The band at 144.07 eV was divided into three peaks (143.62, 143.81 and 145.01 eV), which could be assigned to the different chemical bonds, such as Pb-O and Pb-Se, etc. (Zhou *et al.* 2017; Beygi *et al.* 2018; Zhu *et al.* 2019). All the above results confirm that Pb^{2+} was adsorbed on the surface of ZnSe/ZnO/Bio-$CaCO_3$ by ion-exchange.

CONCLUSIONS

An efficient adsorbent of ZnSe/ZnO/Bio-$CaCO_3$ was successfully prepared by a simple thermal hydrolysis method. It appeared as sheet-like microspheres and the specific surface area was about ~28 m^2/g. It could effectively remove Pb^{2+} from the aqueous solutions. It was beneficial to adsorb Pb^{2+} at an initial pH value = 6.5 and the q_{max} could reach 1,424.78 mg/g at room temperature. It was superior to many of the reported adsorbent materials. The pseudo-second-order model could well fit the adsorption kinetics and ion exchange played an important role in the adsorption process. It provides an effective way for the recycling of biomass.

ACKNOWLEDGEMENTS

The authors are grateful to the Applied Basic Research Programs of Science and Technology Department of Sichuan Province (2018JY0115), the Application Technology

Research and Development Special Project of Nanchong, China (18YFZJ0035), the Meritocracy Research Funds of China West Normal University (17YC013, 17YC139).

CONFLICTS OF INTEREST

The authors declare no conflicts of interest.

SUPPLEMENTARY MATERIAL

The Supplementary Material for this paper is available online at https://dx.doi.org/10.2166/wst.2020.081.

REFERENCES

Beygi, H., Sajjadi, S. A., Babakhani, A., Young, J. F. & van Veggel, F. C. J. M. 2018 Halide-, hybrid-, and perovskite-functionalized light absorbing quantum materials of p–i–n heterojunction solar cells. *ACS Appl. Mater. Inter.* **10** (36), 30283–30295.

Chavan, A. A., Li, H., Scarpellini, A., Marras, S., Manna, L., Athanassiou, A. & Fragouli, D. 2015 Elastomeric nanocomposite foams for the removal of heavy metal ions from water. *ACS Appl. Mater. Interfaces* **7** (27), 14778–14784.

Chen, D., Shen, W., Wu, S., Chen, C., Luo, X. & Guo, L. 2016 Ion exchange induced removal of Pb(ii) by MOF-derived magnetic inorganic sorbents. *Nanoscale* **8** (13), 7172–7179.

Chen, W., Lu, Z., Xiao, B., Gu, P., Yao, W., Xing, J., Asiri, A. M., Alamry, K. A., Wang, X. & Wang, S. 2019 Enhanced removal of lead ions from aqueous solution by iron oxide nanomaterials with cobalt and nickel doping. *J. Clean. Prod.* **211**, 1250–1258.

Choi, J.-S., Trinh, T. X., Yoon, T.-H., Kim, J. & Byun, H.-G. 2019 Quasi-QSAR for predicting the cell viability of human lung and skin cells exposed to different metal oxide nanomaterials. *Chemosphere* **217**, 243–249.

De Angelis, G., Medeghini, L., Conte, A. M. & Mignardi, S. 2017 Recycling of eggshell waste into low-cost adsorbent for Ni removal from wastewater. *J. Clean. Prod.* **164**, 1497–1506.

Dong, Q., Guo, X., Huang, X., Liu, L., Tallon, R., Taylor, B. & Chen, J. 2019 Selective removal of lead ions through capacitive deionization: role of ion-exchange membrane. *Chem. Eng. J.* **361**, 1535–1542.

Fu, W. & Huang, Z. Q. 2018 One-pot synthesis of a two-dimensional porous Fe_3O_4/Poly($C_3N_3S_3$) network nanocomposite for the selective removal of Pb(II) and Hg(II) from synthetic wastewater. *ACS Sustain. Chem. Eng.* **6** (11), 14785–14794.

Gao, H., Du, J. & Liao, Y. J. C. 2019 Removal of chromium(VI) and orange II from aqueous solution using magnetic polyetherimide/sugarcane bagasse. *Cellulose* **26** (5), 3285–3297.

Karthik, R. & Meenakshi, S. 2015 Removal of Pb(II) and Cd(II) ions from aqueous solution using polyaniline grafted chitosan. *Chem. Eng. J.* **263**, 168–177.

Li, F., Wang, X., Yuan, T. & Sun, R. 2016 A lignosulfonate-modified graphene hydrogel with ultrahigh adsorption capacity for Pb(II) removal. *J. Mater. Chem. A* **4** (30), 11888–11896.

Li, R. H., Deng, H. X., Zhang, X. F., Wang, J. J., Awasthi, M. K., Wang, Q., Xiao, R., Zhou, B. Y., Du, J. & Zhang, Z. Q. 2019a High-efficiency removal of Pb(II) and humate by a CeO_2-MoS_2 hybrid magnetic biochar. *Bioresour. Technol.* **273**, 335–340.

Li, Y. T., Song, S. X., Xia, L., Yin, H. Q., Meza, J. V. G. & Ju, W. M. 2019b Enhanced Pb(II) removal by algal-based biosorbent cultivated in high-phosphorus cultures. *Chem. Eng. J.* **361**, 167–179.

Liu, X., Lai, D. & Wang, Y. 2019 Performance of Pb(II) removal by an activated carbon supported nanoscale zero-valent iron composite at ultralow iron content. *J. Hazard. Mater.* **361**, 37–48.

López-Marzo, A., Pons, J. & Merkoçi, A. 2012 Controlled formation of nanostructured $CaCO_3$–PEI microparticles with high biofunctionalizing capacity. *J. Mater. Chem.* **22** (30), 15326–15335.

Ma, A., Abushaikha, A., Allen, S. J. & McKay, G. 2019 Ion exchange homogeneous surface diffusion modelling by binary site resin for the removal of nickel ions from wastewater in fixed beds. *Chem. Eng. J.* **358**, 1–10.

Manos, M. J. & Kanatzidis, M. G. 2016 Metal sulfide ion exchangers: superior sorbents for the capture of toxic and nuclear waste-related metal ions. *Chem. Sci.* **7** (8), 4804–4824.

Mehdinia, A., Vaighan, D. J. & Jabbari, A. 2018 Cation exchange superparamagnetic Al-based metal organic framework (Fe_3O_4/MIL-96(Al)) for high efficient removal of Pb(II) from aqueous solutions. *ACS Sustain. Chem. Eng.* **6** (3), 3176–3186.

Pettinato, M., Chakraborty, S., Arafat, H. A. & Calabro, V. 2015 Eggshell: a green adsorbent for heavy metal removal in an MBR system. *Ecotoxicol. Environ. Saf.* **121**, 57–62.

Ren, H., Li, B., Neckenig, M., Wu, D., Li, Y., Ma, Y., Li, X. & Zhang, N. 2019 Efficient lead ion removal from water by a novel chitosan gel-based sorbent modified with glutamic acid ionic liquid. *Carbohydr. Polym.* **207**, 737–746.

Sarma, D., Malliakas, C. D., Subrahmanyam, K. S., Islam, S. M. & Kanatzidis, M. G. 2016 K2xSn4 – xS8 – x (x = 0.65–1): a new metal sulfide for rapid and selective removal of Cs^+, Sr_2^+ and UO_2^{2+} ions. *Chem. Sci.* **7** (2), 1121–1132.

Seyahmazegi, E. N., Mohammad-Rezaei, R. & Razmi, H. 2016 Multiwall carbon nanotubes decorated on calcined eggshell waste as a novel nano-sorbent: application for anionic dye Congo Red removal. *Chem. Eng. Res. Des.* **109**, 824–834.

Tizo, M. S., Blanco, L. A. V., Cagas, A. C. Q., Dela Cruz, B. R. B., Encoy, J. C., Gunting, J. V., Arazo, R. O. & Mabayo, V. I. F. 2018 Efficiency of calcium carbonate from eggshells as an adsorbent for cadmium removal in aqueous solution. *Sustain. Environ. Res.* **28** (6), 326–332.

Venkateswarlu, S. & Yoon, M. 2015 Core-shell ferromagnetic nanorod based on amine polymer composite (Fe_3O_4@DAPF) for fast removal of Pb(II) from aqueous solutions. *ACS Appl Mater Interfaces* **7** (45), 25362–25372.

Wang, H., Gao, B., Fang, J., Ok, Y. S., Xue, Y., Yang, K. & Cao, X. 2018a Engineered biochar derived from eggshell-treated biomass for removal of aqueous lead. *Ecol. Eng.* **121**, 124–129.

Wang, J., Zhang, Q., Shao, X., Ma, J. & Tian, G. 2018b Properties of magnetic carbon nanomaterials and application in removal organic dyes. *Chemosphere* **207**, 377–384.

Xu, H., Li, L., Lv, H., Liu, X. & Jiang, H. 2016 pH-dependent phosphatization of ZnO nanoparticles and its influence on subsequent lead sorption. *Environ. Pollut.* **208** (Pt B), 723–731.

Yan, L. L., Kong, L., Qu, Z., Lo, L. & Shen, G. Q. 2015 Magnetic Biochar decorated with ZnS nanocrystals for Pb (II) removal. *ACS Sustain. Chem. Eng.* **3** (1), 125–132.

Yang, X., Wan, Y., Zheng, Y., He, F., Yu, Z., Huang, J., Wang, H., Ok, Y. S., Jiang, Y. & Gao, B. 2019 Surface functional groups of carbon-based adsorbents and their roles in the removal of heavy metals from aqueous solutions: a critical review. *Chem. Eng. J.* **366**, 608–621.

Yin, L., Yang, X., Xing, Y., Lu, P., Tsai, C.-J., Attoui, M., Cui, Y., Liu, Y. & Li, Z. 2019 Removal of ultrafine particles by porous nanomaterials with varied morphologies. *Powder Technol.* **342**, 380–387.

Yuan, K., Lee, S. S., De Andrade, V., Sturchio, N. C. & Fenter, P. 2016 Replacement of calcite ($CaCO_3$) by cerussite ($PbCO_3$). *Environ. Sci. Technol.* **50** (23), 12984–12991.

Zhang, L., Zhang, L., Wu, T., Jing, X., Li, R., Liu, J., Liu, Q. & Wang, J. 2015 In situ growth of ZnO nanorod arrays on cotton cloth for the removal of uranium(vi). *Rsc. Adv.* **5** (66), 53433–53440.

Zhang, J., Yao, B., Ping, H., Fu, Z., Li, Y., Wang, W., Wang, H., Wang, Y., Zhang, J. & Zhang, F. 2016 Template-free synthesis of hierarchical porous calcium carbonate microspheres for efficient water treatment. *RSC Adv.* **6** (1), 472–480.

Zhang, T., Tu, Z., Lu, G., Duan, X., Yi, X., Guo, C. & Dang, Z. 2017 Removal of heavy metals from acid mine drainage using chicken eggshells in column mode. *J. Environ. Manage.* **188**, 1–8.

Zhang, L. K., Guo, J. Y., Huang, X. M., Wang, W. D., Sun, P., Li, Y. M. & Han, J. H. 2019 Functionalized biochar-supported magnetic $MnFe_2O_4$ nanocomposite for the removal of Pb(II) and Cd(II). *RSC Adv.* **9** (1), 365–376.

Zhou, X., Liu, W., Zhang, J., Wu, C., Ou, X., Tian, C., Lin, Z. & Dang, Z. 2017 Biogenic calcium carbonate with hierarchical organic–inorganic composite structure enhancing the removal of Pb(II) from wastewater. *ACS Appl. Mater. Inter.* **9** (41), 35785–35793.

Zhu, H., Yuan, J., Tan, X., Zhang, W., Fang, M. & Wang, X. 2019 Efficient removal of Pb^{2+} by Tb-MOFs: identifying the adsorption mechanism through experimental and theoretical investigations. *Environ. Sci. Nano* **6** (1), 261–272.

First received 27 November 2019; accepted in revised form 12 February 2020. Available online 25 February 2020